





Inverse-perovskites A_3BO ($A = \text{Sr}, \text{Ca}, \text{Eu}/B = \text{Pb}, \text{Sn}$): A platform for control of Dirac and Weyl Fermions

Cite as: APL Mater. **7**, 121114 (2019); <https://doi.org/10.1063/1.5129695>

Submitted: 30 September 2019 . Accepted: 12 December 2019 . Published Online: 31 December 2019

A. W. Rost , J. Kim , S. Suetsugu, V. Abdolazimi, K. Hayama, J. A. N. Bruin, C. Mühle, K. Kitagawa, A. Yaresko, J. Nuss , and H. Takagi 

COLLECTIONS

Paper published as part of the special topic on [Topological Semimetals & New Directions](#)

Note: This paper is part of the Special Topic on Topological Semimetals–New Directions.



View Online



Export Citation



CrossMark

ARTICLES YOU MAY BE INTERESTED IN

[The rise of 2D dielectrics/ferroelectrics](#)


APL Materials **7**, 120902 (2019); <https://doi.org/10.1063/1.5129447>

[Inorganic halide perovskite materials and solar cells](#)

APL Materials **7**, 120702 (2019); <https://doi.org/10.1063/1.5117306>

[Performance boosting strategy for perovskite light-emitting diodes](#)

Applied Physics Reviews **6**, 031402 (2019); <https://doi.org/10.1063/1.5098871>



AMERICAN ELEMENTS

THE ADVANCED MATERIALS MANUFACTURER®

additive manufacturing epitaxial crystal growth cerium oxide polishing powder silver nanoparticles sputtering targets III-IV semiconductors CVD precursors europium phosphors

Li Be gallium lump glassy carbon nanodispersions He

Na Mg surface functionalized nanoparticle: B C N O F Ne

K Ca Sc Ti V Cr Mn Fe Co Ni Cu Zn Ga Ge As Se Kr

Rb Sr Y Zr Nb Mo Tc Ru Rh Pd Ag Cd In Sn Sb Te I Xe

Cs Ba La Hf Ta W Re Os Ir Pt Au Hg Tl Pb Bi Po At Rn

Fr Ra Ac Rf Db Sg Bh Hs Mt Ds Rg Cn Uut Uuq Uuq Uuq Uuq

deposition slugs OLED Lighting spintronics solar energy

osmium nanoribbons thin films chalcogenides AuNPs

GDC Li-ion battery electrolytes 99.999% ruthenium spheres

endoheral fullerenes copper nanoparticles diamond micropowder

CIGS MBE grade materials palladium catalysts flexible electronics

beta-barium borate borosilicate glass dysprosium pellets YBCO

pyrolytic graphite 3d graphene foam indium tin oxide mesoporous silica

raman substrates sapphire windows tungsten carbide InGaAs

barium fluoride carbon nanotubes lithium niobate scandium powder

perovskite crystals yttrium iron garnet alternative energy h-BN

gold nanocubes graphene oxide macromolecules photonics

rhodium sponge fiber optics beamsplitters infrared dyes zeolites

fused quartz metallocenes platinum ink buckyballs Ti-6Al-4V

Now Invent.™
The Next Generation of Material Science Catalogs

www.americanelements.com

American Elements opens up a world of possibilities so you can **Now Invent!**




Over 15,000 certified high purity laboratory chemicals, metals, & advanced materials and a state-of-the-art Research Center. Printable GHS-compliant Safety Data Sheets. Thousands of new products. And much more. All on a secure multi-language 'Mobile Responsive' platform.



Inverse-perovskites A_3BO ($A = \text{Sr, Ca, Eu/B} = \text{Pb, Sn}$): A platform for control of Dirac and Weyl Fermions

Cite as: APL Mater. 7, 121114 (2019); doi: 10.1063/1.5129695
Submitted: 30 September 2019 • Accepted: 12 December 2019 •
Published Online: 31 December 2019



A. W. Rost,^{1,2}  J. Kim,¹  S. Suetsugu,³ V. Abdolazimi,¹ K. Hayama,³ J. A. N. Bruin,^{1,4} C. Mühle,¹ K. Kitagawa,³ A. Yaresko,¹ J. Nuss,¹  and H. Takagi^{1,3,5} 

AFFILIATIONS

¹Max Planck Institute for Solid State Research, Heisenbergstrasse 1, 70569 Stuttgart, Germany

²SUPA, School of Physics and Astronomy, University of St Andrews, North Haugh, St Andrews, Fife KY16 9SS, United Kingdom

³Department of Physics, The University of Tokyo, 7-3-1 Hongo, Bunkyo-ku, Tokyo 113-0033, Japan

⁴High Field Magnet Laboratory (HFML-EFML), Radboud University, 6525 ED Nijmegen, The Netherlands

⁵Institute for Functional Matter and Quantum Technologies, University of Stuttgart, Pfaffenwaldring 57, 70550 Stuttgart, Germany

Note: This paper is part of the Special Topic on Topological Semimetals—New Directions.

ABSTRACT

Bulk Dirac electron systems have attracted strong interest for their unique magnetoelectric properties as well as their close relation to topological (crystalline) insulators. Recently, the focus has been shifting toward the role of magnetism in stabilizing Weyl fermions as well as chiral surface states in such materials. While a number of nonmagnetic systems are well known, experimental realizations of magnetic analogs are a key focus of current studies. Here, we report on the physical properties of a large family of inverse perovskites A_3BO ($A = \text{Sr, Ca, Eu/B} = \text{Pb, Sn}$) in which we are able to not only stabilize 3D Dirac electrons at the Fermi energy but also chemically control their properties. In particular, it is possible to introduce a controllable Dirac gap, change the Fermi velocity, tune the anisotropy of the Dirac dispersion, and—crucially—introduce complex magnetism into the system. This family of compounds therefore opens up unique possibilities for the chemical control and systematic investigation of the fascinating properties of such topological semimetals.

© 2019 Author(s). All article content, except where otherwise noted, is licensed under a Creative Commons Attribution (CC BY) license (<http://creativecommons.org/licenses/by/4.0/>). <https://doi.org/10.1063/1.5129695>

INTRODUCTION

Three dimensional Dirac electrons in condensed matter physics have attracted significant interest^{1–3} due to a range of unusual electric and magnetic properties they display. The most easily accessible phenomena are those arising from the unusual single particle excitation spectrum [Fig. 1(a)], combining a vanishing Fermi wave vector k_F with a finite Fermi velocity v_F . The ratio v_F/k_F is, for example, directly proportional to the mobility μ and diverges in the case of Dirac electrons upon approaching the Dirac point energy ϵ_D . A second more unique class of phenomena are those rooted in the Berry curvature, originating from the inherent pseudospin degree of freedom of Dirac dispersions.³ In addition, Dirac electrons form the starting point for the creation of Weyl fermions

lacking Kramers degeneracy via either (i) time reversal symmetry breaking^{4–11} or (ii) the combined effect of inversion symmetry breaking and spin orbit coupling.¹² A number of “clean” 3D Dirac and Weyl electron systems^{13–18} are known in which Dirac and Weyl fermions exist at the Fermi energy E_F . The current focus is on identifying materials in which Weyl points are stabilized by magnetism^{4–8} with recent observations of key experimental signatures by angular resolved photoemission spectroscopy (ARPES)^{9,10} and scanning tunneling microscopy (STM).¹¹ However, there are only limited material classes in which chemical substitution can be used to, e.g., (i) continuously tune the physical properties of Dirac and Weyl fermions, (ii) study topological phase transitions between, e.g., topologically trivial and nontrivial states, or (iii) from Dirac to Weyl systems.¹⁷

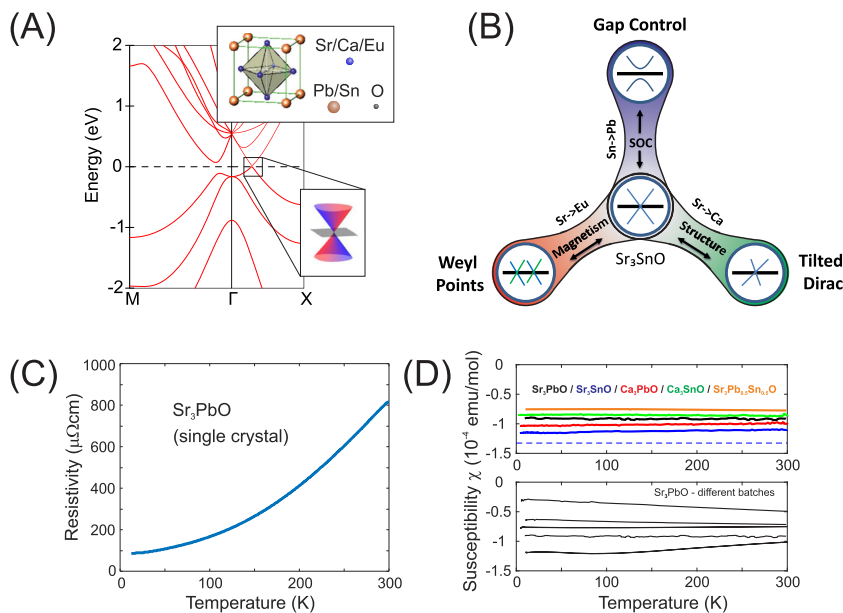


FIG. 1. (a) Band structure of Sr_3PbO . The 3D Dirac point along Γ -X is highlighted. Inset: crystal structure schematic. (b) Possibilities of chemically controlling the properties of Dirac electrons in inverse perovskites. (c) Resistivity as a function of temperature of Sr_3PbO .²² (d) Top: typical magnetic susceptibilities for compounds of the $(\text{Sr,Ca})_3(\text{Sn,Pb})\text{O}$ series. Bottom: magnetic susceptibility as a function of temperature for a number of growth batches of Sr_3PbO .

A very promising candidate family for such studies is tetrel inverse perovskites, A_3BO .¹⁸ A recent detailed synthesis and structure determination study showed that while many members of the series are orthorhombic, an important subset ($A = \text{Ca}, \text{Sr}, \text{Eu}/B = \text{Pb}, \text{Sn}$) is cubic. This is crucial in that only in these cubic systems, a C_4 symmetry axis necessary to protect Dirac points exists.^{19–22} In Fig. 1(a), the inverse perovskite crystal structure and electronic band structure of Sr_3PbO are shown. The general features are common to all nonmagnetic members of the family and have been experimentally confirmed in the case of Ca_3PbO for energies 200 meV below the Dirac point by soft x-ray ARPES.²³ The nominal ionic character is $\text{Sr}^{2+}_3\text{Pb}^{4-}\text{O}^2$. At the Fermi energy, Pb^{4-} states are dominating the valence bands, while Sr^{2+} states dominate the conduction bands. Due to strong spin orbit coupling, these bands overlap at the Γ point by ~ 500 meV. Hybridization opens an angle dependent gap with a maximum value of ~ 200 meV along the Γ -M line. Along the C_4 symmetric Γ -X axis, the gap is effectively zero due to the symmetry properties of the dominant orbital character of the conduction and valence bands at the Fermi energy. This gives rise to 6 symmetry equivalent Dirac points at the gap nodes. The admixture of energetically higher orbitals in combination with spin-orbit-coupling allows in principle for a small Dirac mass gap to open. The band structures of the other members of the family are shown in [supplementary material](#), Sec. 1.

One of the attractive features of this class of materials is the possibility of chemically tuning their properties, as exemplified in Fig. 1(b). Sr_3SnO can be seen as the compound in the series closest to an ideal Dirac system. First of all, the mass gap at the Fermi energy is below that reliably resolvable in *ab initio* calculations (< 10 meV) and currently unresolved in experiments. Second, the Fermi velocities show the lowest anisotropy factor in the series of ~ 1.5 . This low anisotropy marks Sr_3SnO one of the most isotropic Dirac materials compared to, e.g., Na_3Bi or Cd_3As_2 which have anisotropies of order 10.^{13,14} Replacing Sn by Pb increases the role of spin-orbit

coupling at the Fermi energy, giving rise to the opening of a sizeable finite mass gap of at least 20 meV. At the same time, substituting Ca for Sr moves the Dirac point closer to the Γ point, resulting in a significantly stronger anisotropy of the Fermi velocities of up to ~ 4 . We furthermore successfully synthesized intermediate compounds such as $\text{Sr}_3\text{Pb}_{0.5}\text{Sn}_{0.5}\text{O}$, demonstrating the possibility of continuous chemical tuning. Finally, one can introduce magnetism and potentially lift the Kramers degeneracy by replacing Sr/Ca with Eu^{2+} , allowing for the stabilization of Weyl points by time reversal symmetry breaking in the band structure.

In the present study, we make extensive use of magnetization and torque measurements establishing the existence of Dirac electrons at the Fermi energy in Sr_3SnO , Sr_3PbO , Ca_3SnO , and Ca_3PbO . Furthermore, we will present magnetization and magneto-transport data for Eu_3PbO and Eu_3SnO . These unveil localized spin-7/2 moments originating from Eu^{2+} , which order antiferromagnetically at low temperatures with a series of ferrimagnetic and ferromagnetic phases stabilized at a finite magnetic field. Our band structure calculations show that this opens up the possibility for magnetic control of the Dirac- and Weyl-fermion dispersions in Eu_3PbO and Eu_3SnO .

RESULTS

Nonmagnetic compounds $(\text{Sr/Ca})_3(\text{Sn/Pb})\text{O}$

All samples were synthesized, as described in Ref. 18. Due to the air sensitivity of these materials, special precautions are required with more detail given in [supplementary material](#), Sec. 2. The typical product consists of crystallites with sizes of less than $50 \mu\text{m}$ with a few crystals per batch as large as $500 \mu\text{m}$. We confirmed that the large crystallites are indeed the target phase and not a minority phase via single crystal x-ray diffraction. In the case of Sr_3PbO , which yielded the biggest crystallites, we performed single crystal

magneto-transport measurements. In Fig. 1(c), we show a typical resistivity curve.²² While these data and more detailed results are reported elsewhere,²² the most relevant point here is that all as-grown single crystals showed metallic transport. Typical room temperature resistivities are of the order of $700 \mu\Omega \text{ cm}$, and residual resistivity ratios of 5–10 were achieved. Hall measurements are consistent with a holelike carrier concentration of the order of 10^{18} cm^{-3} with a Hall mobility of $4.4 \times 10^4 \text{ cm}^2/\text{V s}$,²² both comparable to other Dirac electron materials.^{13–17} For comparison, we performed transport measurements on pressed pellets of powder samples on the $A = \text{Sr}$, $\text{Ca}/B = \text{Pb}$, Sn members of the family. These showed transport behavior consistent with the single crystal measurements (supplementary material, Sec. 3) and previous reports.^{22,24} In Fig. 1(d) upper panel, we present the magnetic susceptibility as a function of temperature for the four different compounds as well as $\text{Sr}_3\text{Pb}_{0.5}\text{Sn}_{0.5}\text{O}$ (corrected for paramagnetic impurities at lowest temperatures). All samples show a roughly temperature independent diamagnetic susceptibility of the order of -10^{-4} emu/mol . In the case of Sr_3PbO , we furthermore show in the lower panel of Fig. 1(d) the result from measurements across several batches. These reveal a significant variation of $\sim \pm 50\%$. The origin of this variation is most likely the difference in carrier concentration in combination with a strongly energy dependent orbital diamagnetism, as discussed below. The general trend is that batches with the largest diamagnetism showed the smallest frequencies in the quantum oscillation experiments discussed below (see supplementary material, Sec. 4), indicating

that susceptibility measurements correlate with the effective Fermi energy in these samples.

Quantum oscillations in magneto-torque

In order to fully establish the existence of Dirac electrons in the nonmagnetic members of the family, we carried out magneto-torque ($\tau = M \times H$) measurements in search of quantum oscillations. The primary reason for the choice of technique, previously, e.g., used for Bi,²⁵ is that cubic materials have no intrinsic magnetic torque response. Therefore, there is no intrinsic background signal except that from shape anisotropy of the Fermi surfaces originating from anisotropic Fermi velocities.²⁶ We selected crystallites of $>(100 \mu\text{m})^3$ in size with flat reflective surfaces for these experiments. Single crystal x-ray measurements showed that these surfaces are high symmetry surfaces of predominantly [001] orientation (see supplementary material, Sec. 5).

In Fig. 2(a), we show an example of the resulting torque signal in Sr_3PbO . Throughout the paper, we plot the reduced torque $\tau_{\text{red}} = M \times H/|H| = \tau/H$. The oscillations are clearly discernible, and the identification of minima and maxima can be used to calculate the frequency of these oscillations as $F = 4.6 \text{ T}$. The evolution of the oscillation as a function of applied field direction can be easily followed in torque, as shown in Fig. 2(b) (in order to give equal emphasis to oscillations at all fields we are plotting $d\tau/dH$ in all color plots). Here, the extrema/inflection points for a high

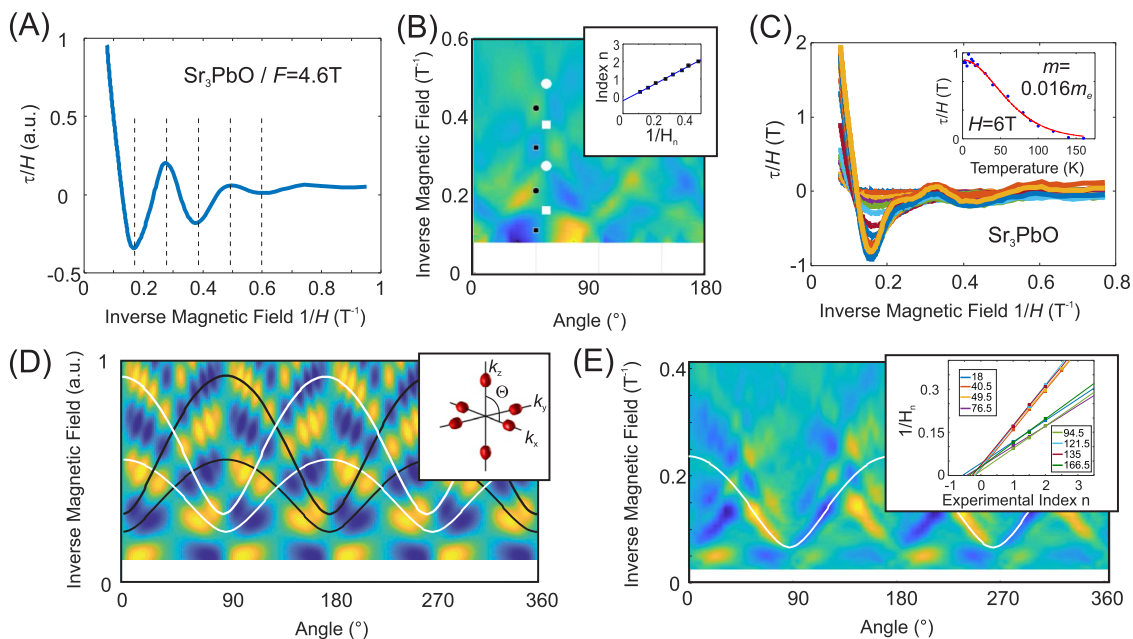


FIG. 2. (a) Quantum oscillations seen in magnetic torque as a function of inverse magnetic field in Sr_3PbO (batch No. 7). Dotted lines indicate extrema. (b) Amplitude of $d\tau/dH$ as a function of magnetic field angle and inverse magnetic field. The symbols mark the locations of extrema close to a high symmetry direction used in the inset, which highlights the linear dependency on inverse magnetic field expected for quantum oscillations. (c) Quantum oscillations as a function of inverse magnetic field for a range of temperatures (see the inset). Inset: amplitude of the oscillatory torque at 6.5 T as a function of temperature. The red line is a Lifshitz-Kosevich fit giving a mass of $m = 0.016m_e$. (d) Simulation of variation of $d\tau/dH$ as a function of inverse magnetic field and angle θ for the Fermi surfaces shown in the inset. The black and white lines highlight angular variation of an extremal orbit originating from two different subsets of the six Fermi surfaces.²² (e) Data of a corresponding measurement on a single crystal of Sr_3PbO with the inset showing the inverse field location of extrema for indexed extrema along a number of high symmetry directions.

symmetry direction are marked with their linear dependence on the inverse magnetic field demonstrated in the inset. Since only few oscillations are traceable, the easiest way to extract an effective mass m^* is to follow the temperature dependence of one of the extrema, as shown in Fig. 2(c). In the inset, we show the amplitude at 6.5 T together with the corresponding Lifshitz-Kosevich fit, giving $m^* = (0.016 \pm 0.001)m_e$.

In order to further elucidate the Fermi surface structure, we studied the angular dependence in more detail. Based on our band structure calculations in combination with the hole-doped character of the magneto-transport,²² the Fermi surfaces should be well described by prolate ellipsoids. Such a model is characterized by a longitudinal (transverse) Fermi momentum $k_{\parallel}(k_{\perp})$ and velocity $v_{\parallel}(v_{\perp})$ along (perpendicular to) the high symmetry Γ -X direction [see the inset of Fig 2(d) and Ref. 22]. Based on these assumptions, we simulated the signal as a function of inverse field and angle. In Fig. 2(d), the result for a rotation of the field in a plane perpendicular to [100] is shown, revealing a characteristic “fingerprint” of the oscillation pattern in $d\tau/dH$. One pair of Fermi surfaces does not contribute due to the fact that the signal is proportional to the gradient of the frequency F with respect to the angle with the applied field Θ , $dF/d\Theta$, which for that pair is zero. The other two pairs of Fermi surfaces contribute equivalent signals which are shifted by 90° [indicated by the white and black dashed lines in Fig. 2(d)], resulting in the characteristic fingerprint. As can be shown by simple geometric arguments, it is possible to determine all characteristic parameters by analysis of the oscillations for two distinct high symmetry angles only (e.g., 0° and 45°). In Fig. 2(e), we show the corresponding experimental results on a single crystal of Sr_3PbO measured for fields up to 33 T at $T = 0.3$ K at the Nijmegen High Field Magnet Laboratory (see supplementary material, Sec. 6 for more details). The angular variation of the extrema (white line) gives a direct measure of the Fermi momentum/Fermi velocity anisotropy which is of order 3 for the samples measured. Analysis of the quantum oscillation frequencies [inset of Fig. 2(e)²²] along high symmetry directions gives Fermi wave vectors of $k_{\parallel} = 0.036 \text{ \AA}^{-1}$, $k_{\perp} = 0.012 \text{ \AA}^{-1}$, respectively. A second sample (supplementary material, Sec. 6) behaves qualitatively identically with $k_{\parallel} = 0.031 \text{ \AA}^{-1}$, $k_{\perp} = 0.010 \text{ \AA}^{-1}$.

We extended these studies to the other three members of the series— Sr_3SnO , Ca_3PbO , and Ca_3SnO . In Figs. 3(a)–3(c), we show representative measurements of τ_{red} as a function of inverse magnetic field for a range of temperatures for each of these materials. Based on the Lifshitz-Kosevich fits to the amplitude shown in the upper inset, these reveal very light masses of $(0.043 \pm 0.002)m_e$, $(0.13 \pm 0.015)m_e$, and $(0.10 \pm 0.01)m_e$ in combination with small average Fermi wave vectors of 0.06 \AA^{-1} , 0.16 \AA^{-1} , and 0.11 \AA^{-1} for Sr_3SnO , Ca_3SnO , and Ca_3PbO , respectively. All materials reveal qualitatively the same characteristic fingerprint of pairs of ellipsoidal Fermi surfaces, as can be deduced from the angular dependency of the quantum oscillations shown in the lower insets of Figs. 3(a)–3(c). Due to the reduced data quality of these lab-based experiments below 14 T, compared to the facility based high field experiments up to 33 T discussed above, a detailed data analysis as in the previous case is not possible.

Magnetic compounds $\text{Eu}_3(\text{Pb/Sn})\text{O}$

We now turn our attention to the Eu based magnetic compounds in this family. In Fig. 4(a), we show the resistivity as a function of temperature measured on pressed powder pellets of Eu_3PbO and Eu_3SnO . At high temperatures, they show metallic behavior similar to the nonmagnetic compounds. However, at ~ 40 K, both materials have a pronounced upturn in resistivity with a sharp drop at lower temperatures. This behavior is consistent with conduction electrons strongly scattering off spin fluctuations at high temperatures which are strongly suppressed in the ordered phase. The temperature dependent magnetic susceptibility χ for both compounds shown in Fig. 4(b) confirms the formation of an antiferromagnetic phase in both compounds. At high temperatures, χ is well described by a Curie Weiss behavior with the appropriate fit yielding a fluctuating magnetic moment of $7.8 \mu_B$ ($8.0 \mu_B$) for Eu_3PbO (Eu_3SnO) with a Weiss temperature of 36.5 K (43.3 K), indicating predominant ferromagnetic correlations. Nevertheless, Eu_3PbO (Eu_3SnO) undergoes a phase transition to an antiferromagnetic state at $T_N = 42.9$ K (33.2 K) as evidenced by the sharp drop in susceptibility at the transition temperature. Measurements of the magnetization as a function

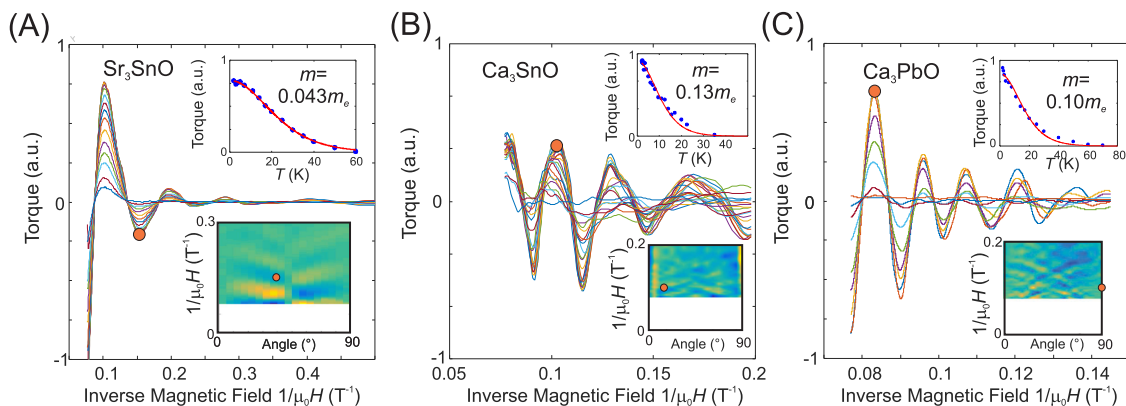


FIG. 3. Quantum oscillations in magnetic torque as a function of inverse magnetic field for Sr_3SnO (a), Ca_3SnO (b), and Ca_3PbO (c). Lower inset: angular variation of $d\tau/dH$ for different magnetic field directions. Upper inset: temperature dependence of amplitude at select points highlighted in lower insets together with a Lifshitz-Kosevich fit. The effective masses are $(0.043 \pm 0.002)m_e$ (Sr_3SnO), $(0.13 \pm 0.015)m_e$ (Ca_3SnO), and $(0.10 \pm 0.01)m_e$ (Ca_3PbO).

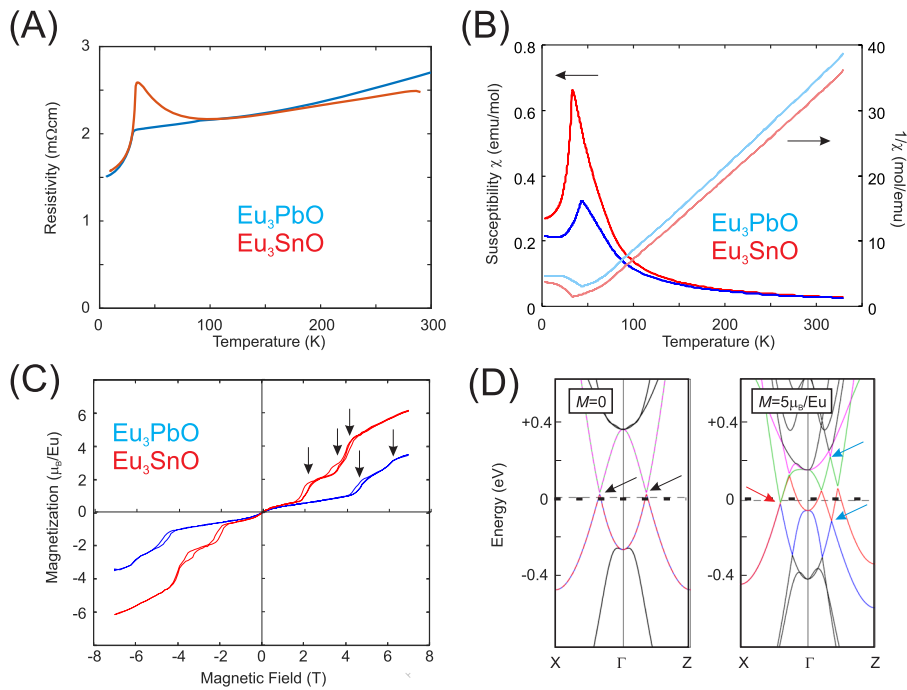


FIG. 4. (a) Resistivity as a function of temperature for pressed polycrystalline pellets of Eu₃PbO and Eu₃SnO. (b) Magnetic susceptibility/inverse magnetic susceptibility as a function of temperature for Eu₃PbO and Eu₃SnO. (c) Magnetization as a function of the magnetic field of polycrystalline samples of Eu₃PbO and Eu₃SnO with transitions highlighted. (d) Band structure calculations for Eu₃PbO in the paramagnetic phase (left) and for moments aligned (001) (right).

of magnetic field at the lowest temperature [Fig. 4(c)] on powder samples reveal a complicated phase diagram, the details of which are outside the scope of this paper. The most relevant point here is that in both compounds, a series of similar magnetization steps is observed, with the transition fields in the Pb compound differing from those in Sn by a factor of 2. In Eu₃SnO, the fully polarized state is reached at ~4 T.

Without detailed knowledge of the arrangement of these magnetic moments, no definite statement on the band structure in the antiferromagnetic and ferrimagnetic phases is possible. However, a band structure calculation is possible assuming localized Eu moments for both the paramagnetic ($M = 0$) and the fully polarized phases with moments along [001]. The results are presented in Fig. 4(d) for high symmetry directions. The paramagnetic phase on the left-hand side shows a band structure qualitatively identical to that of the 3D Dirac compounds discussed above. Contrary to this, the polarized phase exhibits a strongly lifted Kramers degeneracy due to time reversal symmetry breaking. Plotting the band dispersion for momentum directions parallel (Γ -Z) and perpendicular (Γ -X) to the applied field unveils widely differing band structures emerging from Dirac points now located at crystallographically distinct k -points. The positions of Weyl points are marked by blue arrows. The point marked by a red arrow corresponds to an effectively threefold degenerate point (lifted by spin-orbit coupling).

DISCUSSION

Our resistivity measurements reveal all cubic tetrel inverse perovskites studied by us to be metallic, with magnitudes indicating low carrier concentrations consistent with a doped narrow gap

semiconductor. For (Ca/Sr)₃(Pb/Sn)O, this is fully confirmed by the magnetic susceptibility. All samples showed a nearly temperature independent diamagnetic susceptibility of close to -1×10^{-4} emu/mol. This magnitude is of the order of the intrinsic core diamagnetism expected and therefore excludes any large Pauli paramagnetic contribution from free carriers.

What is surprising, however, is the strong variation of the magnetism with carrier concentration that becomes apparent in our measurements on several batches of Sr₃PbO [Fig. 1(d)]. Comparing the frequencies observed in quantum oscillation experiments with band structure calculations²² places the Fermi energies at approximately -70 meV (batch No. 7), -100 meV (batch No. 20) and -130 meV (batch No. 75). If one naively assumed Pauli paramagnetism with a Wilson ratio of 1, this would result in a change in χ of less than 10^{-5} emu/mol, inconsistent with the observed changes. A natural candidate to explain this discrepancy is the giant orbital diamagnetism predicted theoretically²¹ to vary by approximately 1×10^{-4} emu/mol if the Fermi energy differs from the Dirac point energy. Alternatively, an enhanced spin g factor could lead to an enhanced Zeeman splitting. To further disentangle spin and orbital contributions to the magnetism, detailed NMR measurements will be carried out in future studies.

Let us now turn our attention to the magneto-torque measurements. Here, we showed that the angular dependency of the observed quantum oscillations is consistent with prolate ellipsoid Fermi surfaces. For the Sr₃PbO sample shown in Fig. 2(e), the observed Fermi velocity anisotropy is ~ 3 , consistent with the band structure predictions. The measurement of the effective mass m^* allows us to simultaneously determine the Dirac electron velocity $v_F = \hbar k_F / m^*$ and Dirac energy $E_D = \hbar k_F v_F$ ²² [for the sample shown in Fig. 2(c), an average $v_F \approx 5 \times 10^5$ m/s and $k_F \approx 0.01 \text{ \AA}^{-1}$

correspond to a Fermi energy of approximately -70 meV]. To appreciate this combination of Fermi velocities and momenta, it is worth noting that these are comparable to those observed in Cd_3As_2 (see, e.g., Ref. 13). This is in stark contrast to a low doped semiconductor such as SrTiO_3 which for similar Fermi momenta has Fermi velocities approximately two orders of magnitude smaller.²⁷ This is ultimately the source of the anomalously large observed mobilities $\mu \propto v_F/k_F$ since v_F/k_F diverges as $1/(\epsilon - \epsilon_D)$ for Dirac systems but is constant in conventional semiconductors. Furthermore, since no features inconsistent with our assumptions, or higher frequencies indicating further bands, are observed, this allows us to calculate the overall carrier concentration n in these samples. Assuming six spin-degenerate Fermi surfaces, as shown in the inset of Fig. 2(c), we find $n = 7 \times 10^{17}$ for the sample shown in Fig. 2(e) and $n = 3.5 \times 10^{17} \text{ cm}^{-3}$ for a second sample measured by us (see [supplementary material](#), Sec. 6).

A further key quantity of quantum oscillations is their phase, which should be π for an ungapped Dirac electron material, reflecting the intrinsic Berry curvature of the band structure. In the case of a finite mass gap at the Dirac point combined with particle-hole-symmetry breaking of the dispersion, a deviation from this ideal value is possible. For a simple model Hamiltonian, the deviation of the quantum oscillation phase from quantization has been shown, for example, in Ref. 28. In general, the total phase is influenced by a combination of Berry phase, orbital moment, and Zeeman splitting. A detailed discussion has recently been provided by Alexandradinata *et al.*²⁹ The phase deduced by us is clearly angle dependent as can be seen, e.g., from the angle dependent intercept of the fits to the oscillation indices in the inset of Fig. 2(e) (analysis for a second sample is shown in [supplementary material](#), Sec. 6). Note that while it is not straightforward to extract the absolute phase from oscillations in torque, here we solely focus in variations with angle. A careful examination of the band structure in our density functional theory (DFT) calculation however reveals that our Fermi energy of only ~ -70 meV is already sufficiently large for deviations from linearity (indicative of effective particle-hole symmetry breaking) to occur in some momentum directions ([supplementary material](#), Sec. 1). This is the most likely source of the observed angle dependence of the phase.^{28,29} Finally, for Sr_3PbO , we should comment that in our cleanest samples, we reach the ultraquantum limit in which all carriers reside in the lowest Landau level at approximately 10 T, yet we do not observe any signatures indicating new physics for fields up to 33 T.

The same characteristics are qualitatively observed in Sr_3SnO , Ca_3PbO , and Ca_3SnO . While the measured quantum oscillation frequencies are higher, indicating larger carrier concentration, the combination of extremely small k_F with very large v_F clearly also puts these compounds into the class of Dirac materials. In combination with the observed angular variations, this broadly confirms the electronic structure predicted by DFT calculations based on which these materials are classified as topological crystalline insulators.^{30,31}

It is known that Dirac electron materials can be turned into Weyl systems if appropriate magnetism is introduced.^{4–11} This motivated the synthesis of the Eu compounds presented above. Our susceptibility and resistivity measurements show that at high temperatures, fluctuating well localized spin-7/2 moments originating from Eu^{2+} ions exist in a metallic environment. Our results

furthermore demonstrate that magnetic order is stabilized at low temperatures. The exact magnetic structure needs to be determined by neutron experiments which is extremely challenging due to the large absorption cross section of Eu. However, the field dependent measurements show that an almost fully polarized phase can be reached within experimentally accessible limits. Here, our band structure calculations predict a splitting into two Weyl points for Dirac points along the field direction and the stabilization of three-fold degenerate points at the remaining Dirac points. Such a phase naturally has Fermi arc dispersions on surfaces¹² opening the possibility of magnetic control of a chiral surface state. Intriguingly, this fully polarized phase is reached from the zero-field antiferromagnetic state via several intermediate ferrimagnetic phases of as yet undetermined topological character. Detailed magnetization and magneto-transport measurements together with neutron scattering and potentially magnetic field dependent STM studies are required to further investigate the complex phase diagram and topological nature of the phase transitions indicated by the field dependent magnetization.

CONCLUSION

In conclusion, we have established tetrel inverse perovskites as a rich playground for Dirac and Weyl physics. These materials allow for unprecedented chemical control of Dirac electron properties. Together with the possibility of thin film growth,³² this is an important step in exploring the possibility of controlling Dirac physics in this family and, in particular, the consequences of topological phase transitions such as the evolution from Dirac to Weyl Fermion physics in Eu based compounds. For these, we unveiled a complex series of magnetic phases at low temperatures allowing for the evolution of an antiferromagnetic to a fully polarized phase via at least two further (ferri-) magnetic phases. The full determination of the phase diagram together with a determination of the magnetic structures will be an important contribution to this fast-developing field.

SUPPLEMENTARY MATERIAL

See the [supplementary material](#) for (i) band structure details; (ii) sample preparation, handling, and storage; (iii) transport measurements; (iv) quantum oscillation measurements on further samples; (v) single crystal orientation measurements; and (vi) further details on magneto-torque measurements in high magnetic fields.

ACKNOWLEDGMENTS

We would like to thank T. Kariyado, A. Schnyder, Y. Shirai, M. G. Yamada, and M. Ogata for discussions.

This work was partly supported by the Japan Society for the Promotion of Science (JSPS) KAKENHI (Grant Nos. 24224010, 15K13523, JP15H05852, JP15K21717, and 17H01140), EPSRC (Grant No. EP/P024564/1), and the Alexander von Humboldt Foundation. Part of this work was done at the High-Field Magnet Laboratory (HFML-RU/NWO), member of the European Magnetic Field Laboratory (EMFL).

REFERENCES

- ¹S. M. Young, S. Zaheer, J. C. Y. Teo, C. L. Kane, E. J. Mele, and A. M. Rappe, *Phys. Rev. Lett.* **108**, 140405 (2012).
- ²O. Vafek and A. Vishwanath, *Annu. Rev. Condens. Matter Phys.* **5**, 83–112 (2014).
- ³T. O. Wehling, A. M. Black-Schaffer, and A. V. Balatsky, *Adv. Phys.* **63**, 1–76 (2014).
- ⁴D. Bulmash, C.-X. Liu, and X.-L. Qi, *Phys. Rev. B* **89**, 081106 (2014).
- ⁵M. Hirschberger, S. Kushwaha, Z. Wang, Q. Gibson, S. Liang, C. A. Belvin, B. Bernevig, R. Cava, and N. Ong, *Nat. Mater.* **15**, 1161–1165 (2016).
- ⁶Z. Wang, M. Vergniory, S. Kushwaha, M. Hirschberger, E. Chulkov, A. Ernst, N. Ong, R. J. Cava, and B. A. Bernevig, *Phys. Rev. Lett.* **117**, 236401 (2016).
- ⁷S. Borisenko, D. Evtushinsky, Q. Gibson, A. Yaresko, T. Kim, M. Ali, B. Buechner, M. Hoesch, and R. Cava, *Nat. Commun.* **10**, 3424 (2019).
- ⁸L. M. Schoop, A. Topp, J. Lippmann, F. Orlandi, L. Muehler, M. G. Vergniory, Y. Sun, A. W. Rost, V. Duppe, M. Krivenkov, S. Sheoran, P. Manuel, A. Varykhalov, B. Yan, R. K. Kremer, C. R. Ast, and B. V. Lotsch, *Sci. Adv.* **4**, eaar231 (2018).
- ⁹D. F. Liu, A. J. Liang, E. K. Liu, Q. N. Xu, Y. W. Li, C. Chen, D. Pei, W. J. Shi, S. K. Mo, P. Dudin, T. Kim, C. Cacho, G. Li, Y. Sun, L. X. Yang, Z. K. Liu, S. S. P. Parkin, C. Felser, and Y. L. Chen, *Science* **365**, 1282 (2019).
- ¹⁰I. Belopolski, K. Manna, D. S. Sanchez, G. Chang, B. Ernst, J. Yin, S. Zhang, T. Cochran, N. Shumiya, H. Zheng, B. Singh, G. Bian, D. Multer, M. Litskevich, X. Zhou, S.-M. Huang, B. Wang, T.-R. Chang, S.-Y. Xu, A. Bansil, C. Felser, H. Lin, and M. Zahid Hasan, *Science* **365**, 1278 (2019).
- ¹¹N. Morali, R. Batabyal, P. K. Nag, E. Liu, Q. Xu, Y. Sun, B. Yan, C. Felser, N. Avraham, and H. Beidenkopf, *Science* **365**, 1286 (2019).
- ¹²M. Zahid Hasan, S.-Y. Xu, I. Belopolski, and S.-M. Huang, *Annu. Rev. Condens. Matter Phys.* **8**, 289–309 (2017).
- ¹³Z. Wang, Y. Sun, X.-Q. Chen, C. Franchini, G. Xu, H. Weng, X. Dai, and Z. Fang, *Phys. Rev. B* **85**, 195320 (2012).
- ¹⁴A. Narayanan, M. D. Watson, S. F. Blake, N. Bruyant, L. Drigo, Y. L. Chen, D. Prabhakaran, B. Yan, C. Felser, T. Kong, P. C. Canfield, and A. I. Coldea, *Phys. Rev. Lett.* **114**, 117201 (2015).
- ¹⁵M. Novak, S. Sasaki, K. Segawa, and Y. Ando, *Phys. Rev. B* **91**, 041203 (2015).
- ¹⁶R. Y. Chen, S. J. Zhang, J. A. Schneeloch, C. Zhang, Q. Li, G. D. Gu, and N. L. Wang, *Phys. Rev. B* **92**, 075107 (2015).
- ¹⁷P. Dziawa, B. J. Kowalski, K. Dybko, R. Buczko, A. Szczerbakow, M. Szot, E. Lusakowska, T. Balasubramanian, B. M. Wojek, M. H. Berntsen, O. Tjernberg, and T. Story, *Nat. Mater.* **11**, 1023 (2012).
- ¹⁸J. Nuss, C. Mühle, K. Hayama, V. Abdolazimi, and H. Takagi, *Acta Crystallogr., Sect. B: Struct. Sci.* **71**, 300 (2015).
- ¹⁹T. Kariyado and M. Ogata, *J. Phys. Soc. Jpn.* **80**, 083704 (2011).
- ²⁰T. Kariyado and M. Ogata, *J. Phys. Soc. Jpn.* **81**, 064701 (2012).
- ²¹T. Kariyado, Ph.D. thesis, University of Tokyo, 2012.
- ²²S. Suetsugu, K. Hayama, A. W. Rost, J. Nuss, C. Mühle, J. Kim, K. Kitagawa, and H. Takagi, *Phys. Rev. B* **98**, 115203 (2018).
- ²³Y. Obata, R. Yukawa, K. Horiba, H. Kumigashira, Y. Toda, S. Matsuishi, and H. Hosono, *Phys. Rev. B* **96**, 155109 (2017).
- ²⁴M. Oudah, A. Ikeda, J. N. Hausmann, S. Yonezawa, T. Fukumoto, S. Kobayashi, M. Sato, and Y. Maeno, *Nat. Commun.* **7**, 13617 (2016).
- ²⁵L. Li, J. G. Checkelsky, Y. S. Hor, C. Uher, A. F. Hebard, R. J. Cava, and N. P. Ong, *Science* **321**, 547–550 (2008).
- ²⁶D. Shoenberg, *Magnetic Oscillations in Metals* (Cambridge University Press, 2009).
- ²⁷X. Lin, Z. Zhu, B. Fauque, and K. Behnia, *Phys. Rev. X* **3**, 021002 (2013).
- ²⁸A. A. Taskin and Y. Ando, *Phys. Rev. B* **84**, 035301 (2011).
- ²⁹A. Alexandradinata, C. Wang, W. Duan, and L. Glazman, *Phys. Rev. X* **8**, 011027 (2018).
- ³⁰T. H. Hsieh, J. Liu, and L. Fu, *Phys. Rev. B* **90**, 081112 (2014).
- ³¹C.-K. Chiu, Y.-H. Chan, X. Li, Y. Nohara, and A. P. Schnyder, *Phys. Rev. B* **95**, 035151 (2017).
- ³²D. Samal, H. Nakamura, and H. Takagi, *APL Mater.* **4**, 076101 (2016).